Observations of the Roots of Plasma Bubbles: Are They Sometimes Foamy?

Charles L. Bennett[1]

[1]Lawrence Livermore National Laboratory (retired).

Corresponding author: Charles Bennett (Charlie_Bennett@comcast.net)

Key Points:

- Dispersionless, highly attenuated, lightning generated electromagnetic waves are observed in the lower ionosphere
- The propagation of these electromagnetic waves has characteristics of acoustic wave propagation through two-phase foams
- Such foamy plasma bubbles may cover approximately 80% of the bottomside of the equatorial nightside ionosphere.

Abstract

Dramatic irregularities in the plasma density of the ionosphere, first discovered by their effects on radio wave propagation in 1938, and despite decades of investigation, still remain puzzling. Their deleterious effects on radio wave communication, satellite command and control, GPS navigation are serious enough to strongly motivate better understanding of their nature. Many aspects of such irregularities are now understood, but the mechanism(s) of their formation and their detailed nature remain a topic of great interest. In this work, detailed time resolved measurements of lightning generated waves show dispersionless, strongly attenuated propagation with substantial propagation delays. These characteristics of the electromagnetic wave propagation in the two-phase bubble/non-bubble ionosphere parallel the characteristics of acoustic wave propagation through two-phase liquid/vapor foams; and this motivates the suggestion that the bottomside layer of the ionosphere may sometimes be foamy.

Plain Language Summary

Just as ocean waves breaking at the interface between sea and land produce copious bubbles and foam, recent satellite data suggests a similar phenomenon at the interface between neutral atmosphere and the charged plasma of the ionosphere. Lightning generated electromagnetic waves passing through the lower ionosphere observed by low altitude satellites are found to have the same characteristics as acoustic waves passing through foamy water. This hypothetical foam in the lower ionosphere apparently strongly absorbs radio waves and seems to prevent most such waves from escaping the foam to pass through to the upper ionosphere.

1 Introduction

This article is a sequel to (Bennett 2023), that describes a novel method for the observation and analysis of the *roots* of equatorial plasma bubbles (EPBs). Most of the details in (Bennett 2023) will not be repeated here, but a brief summary is presented in the following section 2.

EPBs are localized density depletions (sometimes by over four orders of magnitude relative to the surrounding plasma) in the nighttime equatorial ionosphere (Heelis, 2004; Kil & Heelis, 1998; Woodman and Hoz, 1976). The literature on EPBs is vast and spans nearly a century. Nowadays there is increasing motivation to understand such bubbles and their detrimental affects on radio communications, especially satellite communications, for which “loss of lock” events can be precipitated by their presence. Another detrimental effect is the disruption of signals from the Global Navigation Satellite System so important to modern society. Numerous reviews of the development of the experimental and theoretical understanding of plasma bubbles are available (e.g. Balan, et al. 2018; De Michelis et al. 2021; Huba, 2023; Kelley et al. 2011; Makela & Otsuka 2012; Woodman, 2009).

It is generally accepted that the lower density of plasma bubbles relative to their surroundings causes them to rise in a turbulent process giving rise to plumelike features in radar observations (e.g. Abdu et al., 2012; Hysell et al., 2005; Kelley et al., 2011; Kudeki & Bhttacharyya, 1999; Narayanan et al., 2014; Patra et al., 2005; Tsunoda, 1983; Yokoyama et al., 2011). Plasma bubbles may also be detected as emission depletion bands in optical observations, (e.g., Immel et al., 2003; Kil et al., 2004; Makela & Kelley, 2003; Makela et al., 2006; Makela & Miller, 2008; Martinis et al., 2003; Mendillo & Baumgardner, 1982; Pimenta et al., 2003; Shiokawa et al., 2004). Animations of sequences of optical images, such as those in Makela &

Miller, (2008) most clearly and dramatically show plasma bubbles emerging from low altitudes with subsequent rising and Eastward drifting. Such animations not only show apparent turbulent structures emerging from regions of depleted emission, but also show apparently non-turbulent depleted emission regions extending continuously below the turbulent regions towards the base of the ionosphere. In the present article the term *roots* of plasma bubbles refers to density depletions that extend *contiguously* to the base of the ionosphere that aren't necessarily turbulent.

Initial observations and most early investigations of plasma bubbles involved so-called "spread F" phenomena, in which radar pulses of a given frequency, rather than reflecting from distinct ionospheric layers corresponding to distinct altitudes of reflection were observed to return from a spread out region of altitudes (Woodman, 2009). As such radar reflections require the presence of ionospheric density irregularities at the scale of the radar wavelength, conventional spread F phenomena would not be seen for non turbulent roots of plasma bubbles.

Woodman (2009) states "We implicitly assume that there is a cascade mechanism as proposed by Haerendel (1973) from the larger to the smaller scale, but we do not know exactly how this takes place." Woodman (2009) further states "The current state of the theory is that high frequency drift instabilities can explain the shortest wavelengths, up to ~1 m and the low frequency waves longer than 10 m, but no existing theory can explain the waves around 3 m, i.e., the strong echoes that Jicarmarca sees!"

Kelley (2011) states "How structure can be transferred from 1000 km to 1 m is still a bit of a mystery. Since there is linear growth in the power lay regime, it is not because of an inertial cascade" and "Much remains to be done before the electrodynamics and coupling processes in this region during solar minimu conditions are fully understood."

To this day, the formation of the initial density depletions evidently required to "seed" larger scale turbulent fluctuations responsible for the greatest degradations of radio communications are not fully understood (Chou et al., 2022; De Michelis et al. 2022; Huba, 2023; Kil et al., 2022).

The remainder of this paper is organized as follows: Section 2 provides a summary of the earlier (Bennett 2023) paper involving the detailed description of the data sources and analysis methods relevant to the current work. Section 3 introduces the more detailed analysis for the determination of the wavevector propagation directions, energy propagation directions and intensities, and most significantly, the determination of the dispersiveness of the local plasma medium based on the relation between estimated phase velocity on frequency. This wavevector analysis is applied to a typical whistler previously described in (Bennett 2023). Section 4 then applies this wave vector analysis to some unusually low dispersion events that (Bennett 2023) suggests are characteristic of lightning generated waves observed from a location within a plasma bubble that extends contiguously to the base of the ionosphere, i.e. a plasma root. Section 5 provides a summary discussion and final conclusions for this work.

2 Relevant Highlights of Earlier Work

Figure **3** of (Bennett 2023) provides a concise overview of this earlier work. This figure illustrates schematically the propagation of a lightning generated (LG) electromagnetic pulse (EMP) from the location of a representative lightning strike, through the Earth ionosphere waveguide (EIWG), with penetration into the ionosphere at the EIWG upper boundary

(EIWGUB) and continuing up to the location of Van Allen probe sensors at various times along the satellite orbit. For each of a series of 100 six-second bursts of data, circles are plotted at the satellite location (in geographic latitude and altitude) with diameters proportional to the measured dispersion. Within some bursts unusual dispersionless spikes are observed in scalograms. These spikes are interpreted as the result of LG waves passing through plasma bubbles on their way to the satellite while the satellite is immersed within a bubble. The complete lack of dispersion observed for these spikes is interpreted as evidence that almost no "normal", i.e. bubble free, ionospheric plasma was encountered along the path from lightning strike to satellite for these waves, as otherwise some measureable degree of dispersion would have been seen. The contiguity of the plasma bubble density depletion along the full path from the EIWG to the satellite is suggested by the "roots" designation. It is noted in this figure that "normally dispersed" whistlers and unusual dispersionless spikes are almost never seen at the same time.

In (Bennett 2023) I suggested that the roots of plasma bubbles might sometimes be foamy. This suggestion was made based on the propagation characteristics of LG waves passing through such roots. In Figure **11** of (Bennett 2023), the electric field signals observed by the EMFISIS instruments on the Van Allen probe A satellite at an altitude of 239 km from an especially distinctive lightning flash are shown. Excess propagation delays of 7 to 31 ms were found associated with propagation through the ionospheric plasma for a set of four distinct lightning generated (LG) events. The nearly equal intensities observed in the four electric field peaks, as seen in Figures **11b**, **11d** & **11f** of (Bennett 2023), contrast to the significantly different estimated intensities based on WWLLN measured energies as seen in Figure **11g** of (Bennett 2023). In stark contrast Figure **10** of (Bennett 2023) shows that no excess propagation delay through the Earth ionosphere waveguide (EIWG) was observed for the LG events as detected on the ground WERA network by magnetic field detectors. Also in stark contrast, the relative intensities of all seven events seen both in the WERA data and the WWLLN data shown in Figures **10** of (Bennett, 2023) are approximately consistent between the WERA peaks and WWLLN measured energies.

Despite the substantial propagation delays for the four LG events seen in Figure **11** of (Bennett, 2023), no significant *excess* dispersion beyond that already expected, on the basis of the (Nickolaenko et al., 2004) model, from the propagation through the EIWG from the location of the lightning flash to the subsatellite point was seen. The "foamy" character suggested is by analogy to acoustic wave propagation through foams of liquid/gas phase materials (Pierre et al. 2013) for which the velocity for a given liquid fraction is dispersionless, i.e. the measured wave velocity is independent of frequency. The single lightning flash associated with the Geostationary Lightning Mapper (GLM) groups discussed in Figure **11** of (Bennett, 2023) was quite unusual, in that the four peaks seen in the Van Allen probe data were distinct, well separated and nearly equally intense.

Although the path through the ionosphere taken by the four LG events in Figure **11** of (Bennett, 2023) is unknown, it is no less than a minimum distance of about 150 km corresponding to the directly vertical propagation from the EIWGUB to the satellite. For this distance, the four propagation delays correspond to speeds from 5 Mm/s to 20 Mm/s.

The vast majority of LG events are not as distinctive as the flash discussed above. Applying the "group-to-flash" assignment logic from the GLM (Goodman et al., 2013) to the WWLLN events, over the course of a typical day, specifically 5 October, 2019, it is found that

67% of WWLLN strokes are isolated, while less than 0.4% have four or more strokes occurring near the same location (within 0.15° arc distance) at nearly the same time (within 0.33 seconds between successive events) and at nearly the same intensity (no more than a factor of two from the strongest to weakest). For this reason, there are few LG events for which the systematic variation of the attenuation with the propagation delay may be examined, as was done for the case discussed in (Bennett 2023).

However, even for isolated WWLLN events, the highly variable nature of the propagation delays seen within EPBs may be inferred by the numerous strong spikes seen in scalograms of the electric and magnetic fields that do not correlate closely in time with the expected propagation delay through the EIWG of WWLLN detected events. This lack of temporal correlation can be seen in Figures **8** and **9** of (Bennett 2023) for which every WWLLN detected stroke is plotted with the corresponding expected propagation delay through the EIWG as a vertical dashed line. These predicted WWLLN expected times seldom line up closely with spikes in the electric (or magnetic) scalograms.

The main new results in the current work involve the detailed wavevector analysis of both dispersed (i.e. whistlers) and unusually low dispersion waves. Normally dispersed waves are first discussed in section 3. Then in section 4 an extensive discussion of the unusual results from wavevector analysis of the unusually low dispersion waves is presented.

3 Wave Vector Analysis for Normal Whistler Events

3.1 Normal Two Fluid Plasma Dispersion Relations

Figure **1** of the present work shows the two-fluid model dispersion relations from (DeJonge & Keppens 2020a) discussed in Figure **1** of (Bennett 2023), but shown over a broader frequency range and including all six plasma wave modes possible in a representative two-fluid plasma. Superimposed over the dispersion relation curves in **1a**, **1d** and **1g** are inclined dashed lines corresponding to the four asymptotic regions of constant phase velocity, three for the magnetohydrodynamic (MHD) modes **S**, **A** and **F** in their low frequency limit and one for the two electromagnetic modes **O** and **X** in their high frequency limit. The **O** and **X** modes are those most relevant to ground based radar probing of plasma bubbles. As can be seen in **1a**, **1d** and **1g** these modes are cutoff below approximately 2 MHz and thus wavelengths greater than about 0.1 km do not propagate in this plasma. In contrast, the MHD modes are sensitive to structures having a much larger range of sizes. In particular, **F** mode whistlers in a predominantly Oxygen plasma span wavelengths from 0.1 to 10 km as seen in **1d**.

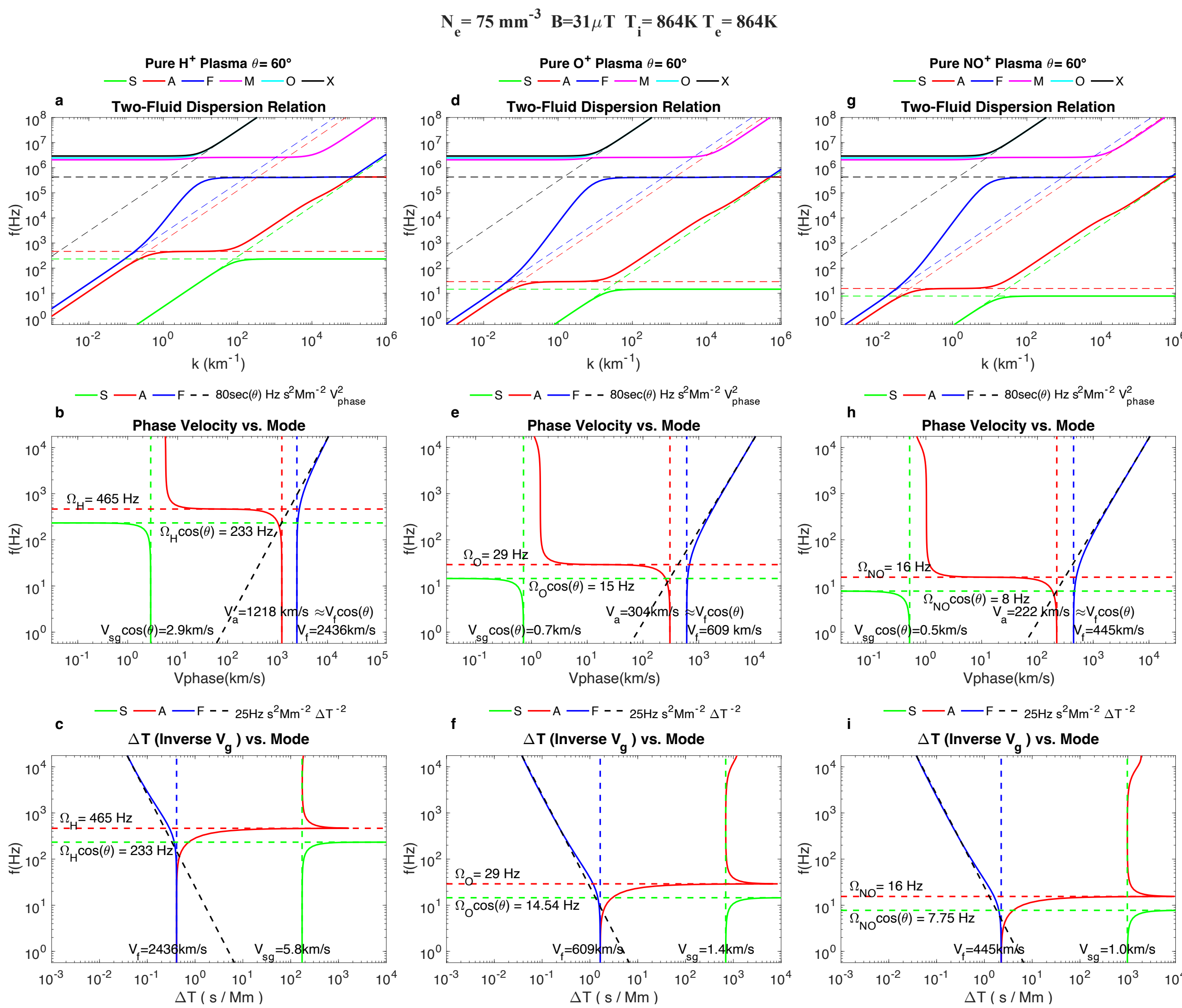

Figure 1. Dispersion relations computed from the De Jonghe and Keppens (2021a) two-fluid model are shown. The plasma parameters in the figure title are typical ionospheric conditions that correspond approximately to the case shown in Figure **5** of (Bennett 2023). The angle between the magnetic field and wavevector direction is θ. The three MHD wave modes are shown in green for **S** slow MS, red for **A** Alfven and blue for **F** fast MS waves; also shown in cyan for **O** ordinary, black for **X** extraordinary electromagnetic and magneta for M modified electrostatic waves. In **a**, **d** and **g**, the wave frequency is shown as a function of the wavenumber for the ion species listed in the legends. The cyclotron frequencies for each ion species are indicated next to the Ω_x labels. In **b**, **e** and **h** the frequency vs. phase velocity V_p is plotted with low frequency limit values for the slow, Alfven and fast velocities (V_s, V_a and V_f) indicated on each plot. In **c**, **f** and **i**, the frequency vs. inverse group velocity V_g is plotted. The dashed lines in **b**, **e**, **h** and **c**, **f**, **g** show that the dispersion constants indicated in the legends reasonably fit the whistling regions for all three ion species.

In **1b**, **1e** and **1h** the frequency versus phase velocity of ***F*** waves for frequencies above the relevant ion cyclotron frequency and below the electron cyclotron frequency (classical whistlers) has quadratic behavior with a coefficient that is insensitive to the ion mass, but varies as the secant of the propagation angle θ. Using the IRI model as described in (Bennett 2023) to estimate the plasma parameters: $N_e = 75\ mm^{-3}$, $B = 31\ \mu T$, $T_i = T_e = 864$ K, the frequency vs. phase velocity is predicted to be

$$f = 80 \sec(\theta)\, Hz \frac{s^2}{Mm^2} V_{phase}^2 \ . \tag{1}$$

The coefficient in this expression is insensitive to the values for T_i and Te, but varies approximately in proportion to N_e and the inverse of B. This relation may alternatively be written as

$$V_{phase} = 112\ \frac{km}{s\sqrt{Hz}} \sqrt{\frac{f}{\cos(\theta)}} \quad . \tag{2}$$

By contrast, in **1c**, **1f** and **1i** although the group velocity in the same region still has quadratic behavior insensitive to ion mass it does not depend on the propagation angle. From the same plasma parameters listed above, the frequency vs. group velocity is given by

$$f = 25\ Hz \frac{s^2}{Mm^2} V_{group}^2 \ . \tag{3}$$

The coefficient in this expression is also insensitive to the values for T_i and Te, and varies in proportion to N_e and inversely with B.

These general and characteristic features of the dispersion relations (De Jonghe & Keppens 2021b) are seen in observational data for whistlers in "normal" plasma regions, but are *violated* in regions of unusual dispersion. In the next subsection, observations for normal cases are presented, while in a later section, some examples of unusual behavior are discussed.

3.2 Normal Dispersion Relation Observations

Figure **2** of the present work shows the scalograms from a 1.6 second portion of the scalograms shown in Figure **5** of (Bennett 2023). Superimposed over the scalograms in this figure, the white vertical dashed line shows the arrival time of an LG pulse delayed only by the travel through the EIWG from the WWLLN location of the lighting strike to the subsatellite location at a speed of 235 km/s. The three curved red dashed lines show three dispersion curves having dispersion constants of 0.1, 12.6 and 25.2 $s\sqrt{Hz}$, and having the same arrival time at the subsatellite location as the white dispersionless case.

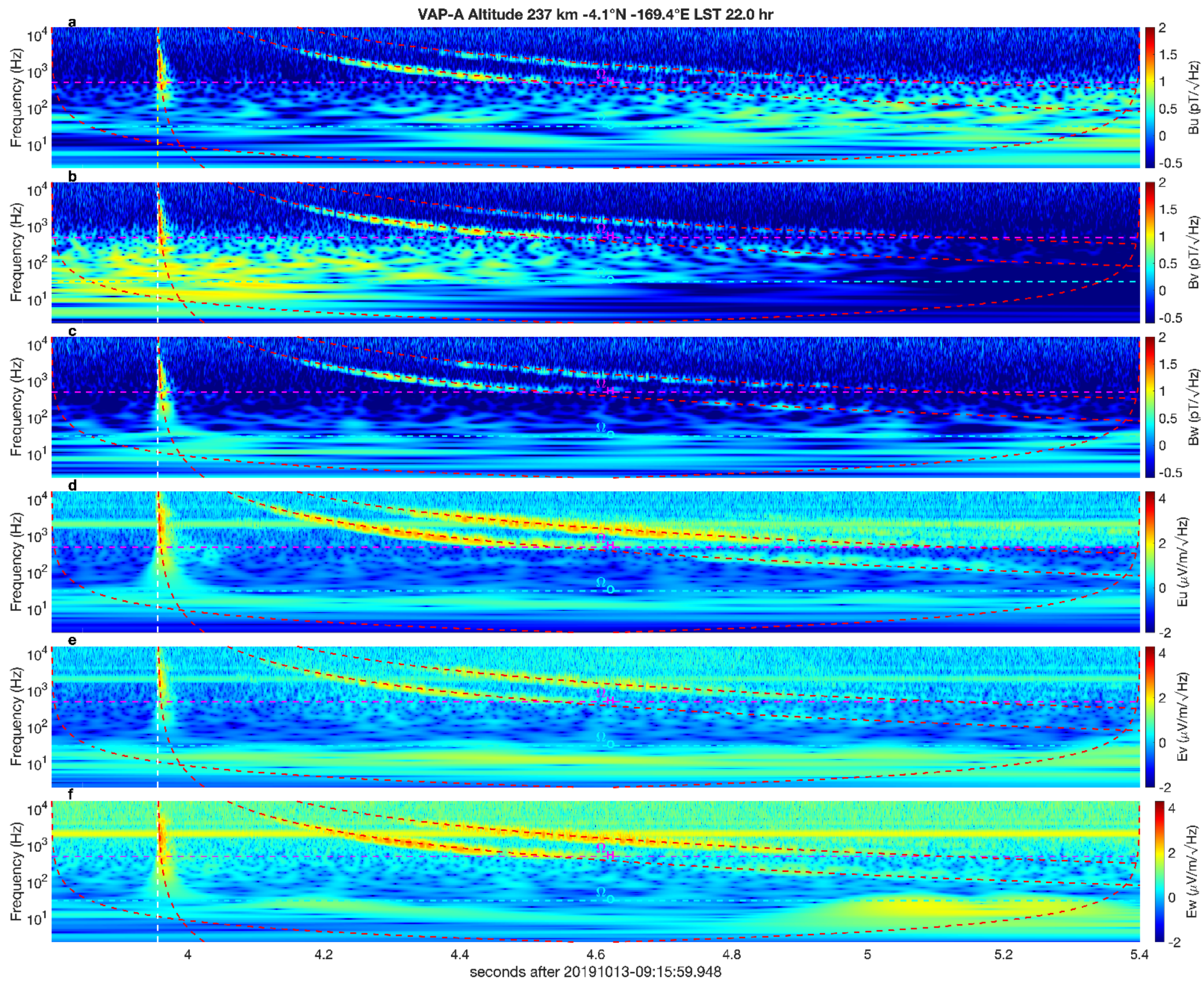

Figure 2. Scalograms of the three magnetic and electric field components in the spinning U,V, W reference frame are displayed for a 1.6 s sample of EMFISIS data. The dashed line curves represent four distinct dispersion constant (DC) values that track the dispersed waves from a single lighting stroke detected by the WWLLN. In **a**, **b** and **c**, scalograms for the Bu, Bv and Bw components of the magnetic field are shown. In **d**, **e** and **f**, scalograms for the Eu, Ev and Ew components of the electric field are shown. The approximate location and local solar time (LST) of the satellite at the time of this data collection is shown in the figure title.

3.3 Wavevector Analysis of Normal Dispersion Observations

Figure **3** of the present work shows a wave vector analysis using the amplitudes along the four superimposed dispersion curves indicated by dashed lines in Figure **2**. At each frequency and time along the dispersion curves having dispersion constant (DC) values indicated in the column titles for Figures **3a**, **3f**, **3k** and **3p**, the complex amplitudes of the scalograms for the electric and magnetic fields are used to compute the Poynting vector

$$\boldsymbol{S}(f) = \boldsymbol{E}(f) \times \boldsymbol{B}^{*}(f) \quad , \tag{4}$$

and the unit Poynting vector

$$\widehat{\boldsymbol{S}}(f) = \boldsymbol{S}(f) \;/\; |\boldsymbol{S}(f)| \quad . \tag{5}$$

The absolute values of the scalar product of the unit Poynting vector with each of the unit vectors in the mean field aligned (MFA) described in (Min, et al. 2017; Ritter, et al. 2013) as a fuction of frequency are shown in the top three rows of Figure **3**. The scalar products along the local magnetic field are indicated by |S•μ| in the ordinate label in **3a**. The scalar products along the magnetic East direction in the horizontal plane are indicated by |S•ϕ| in the ordinate label in **3c**. The scalar products along the direction orthogonal to the first two directions, approximately vertical in the equatorial region, are indicated by |S•ν| in the ordinate label in **3b**. In **3d**, **3i**, **3n** and **3s**, the absolute value of the electric and magnetic field scalogram components are shown as a function of frequency.

Expression 1 is used to estimate the propagation angles θ in the present Figure **3e, 3j, 3o** and **3t** by fitting the high frequency behavior of the four cases. These estimated angles are shown in blue in the last row of Figure **3** and the phase velocity vs. frequency variation of expression 1 is shown by the green line in Figure **3e, 3j, 3o** and **3t** above the oxygen cyclotron frequency. Below the oxygen cyclotron frequency the phase velocity is shown by the horizontal section of the green line at its long wavelength limit assuming the plasma is predominantly O^{+} ions.

As shown in Figure **1**, the long wavelength limiting phase velocity is inversely proportional to the square root of the mass of the dominant plasma constituent. Since the “noise” of other contributions to the scalogram amplitudes along the four dispersion curves is not negligible, significant fluctuations are seen in the estimated Poynting vector projections displayed in the top three rows of Figure **3**. Even so, it seems the direction of the *energy* flow for the low dispersion whistler and its echos are traveling in approximately consistent directions, in contrast to the apparent variation in the direction of the *wavevector* suggested in the last row of Figure **3**. The sign of the propagation direction is irrelevant in the plots of the absolute values of the propagation direction cosines shown in the top three rows of Figure **3**. This whistler and its echos are travelling obliquely in the MFA coordinate system, with unit Poynting vector projections of approximately 0.8, 0.5 and 0.4 along the μ (magnetic field B), ν (~vertical), and ϕ (magnetic East) directions.

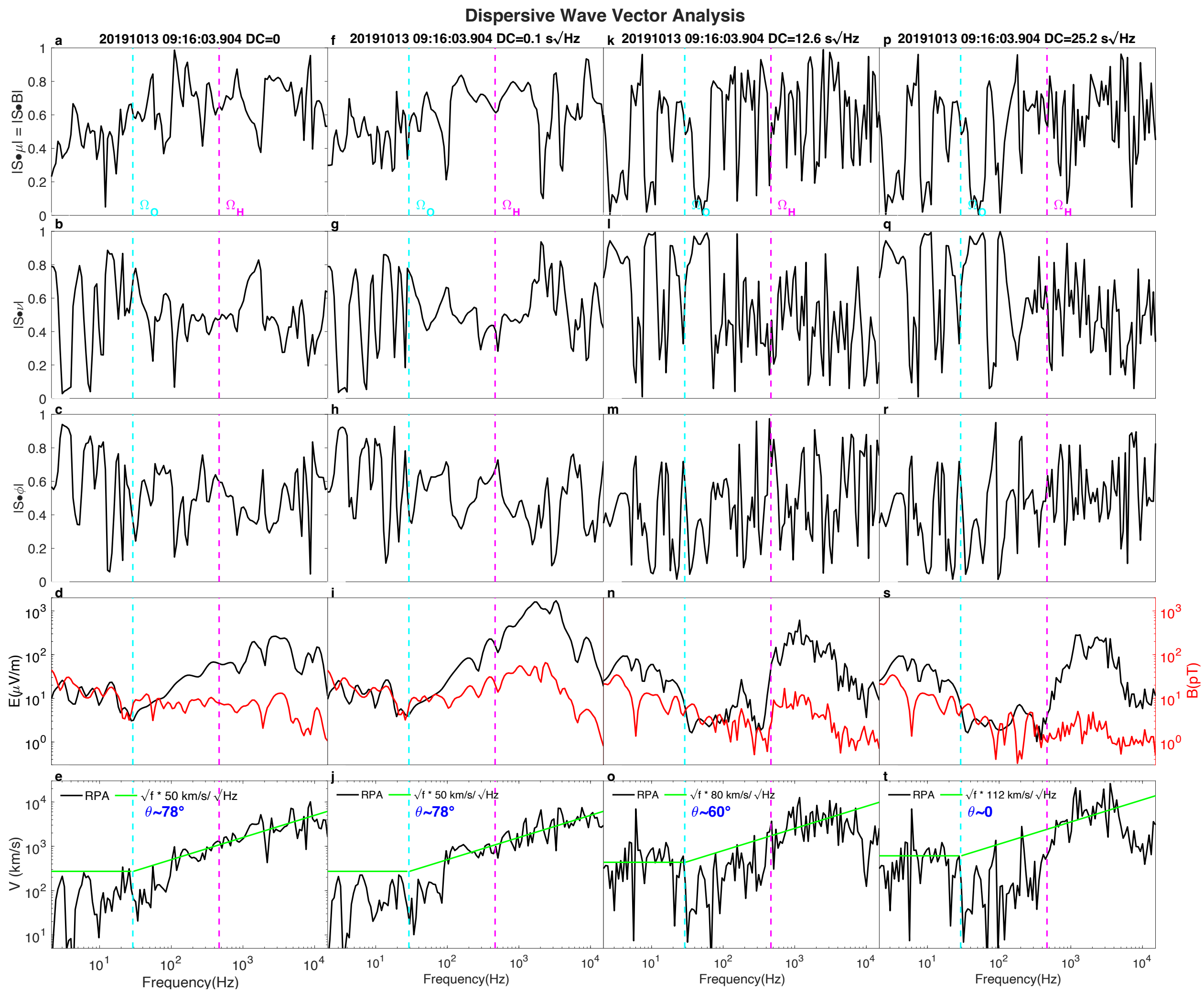

Figure 3. The direction and speed for four different DC values are displayed for the data in the previous figure. In **a**, **f**, **k** and **p**, the absolute values for the projections of the Poynting unit vector S along μ (the direction of the local magnetic field B) are plotted as a function of frequency. Similarly in **b**, **g**, **l** and **q**, projections along the ν direction (approximately vertical) of the MFA coordinate system are shown. Also similarly in **c**, **h**, **m** and **r**, projections along the ϕ direction (magnetic East) of the MFA coordinate system are shown. In **d**, **i**, **n**, **s**, the magnitudes of the electric and magnetic field amplitudes are shown as a function of frequency. In **e**, **j**, **o**, and **t** the RPA estimated phase velocities are plotted as a function of frequency.

Even though the dispersion constant (DC) values are dramatically different for the four cases displayed in Figure **3**, the RPA estimated phase velocities for all four cases are not so different, and are consistent with slightly different cos(θ) angular factors. The reason for the great differences between the DC values is that they represent integrated totals of the dispersion over the full distance (in the last two cases including the echoing path) from source to detector. This sensitivity of the DC values to the integrated dispersion along the full path from source to detection was extensively exploited and discussed in (Bennett 2023). In contrast, the four dispersiveness values seen in **3e**, **3j**, **3o** and **3t** are local measurements, characteristic of the conditions of the ionosphere at the location of the detectors, rather than an integral measure along the full propagation path.

Finally, some measure of the fidelity of the RPA estimates for phase velocity can be judged by the degree to which the scalograms are found to have significant values above the ambient “noise”. For example, for the Bu component displayed in **2a**, scalogram amplitudes for frequencies below 100 Hz appear to decrease to the level of the “background” amplitudes primarily associated with the population of slow magnetosonic waves discussed in (Bennett, 2023). Other components are similarly “lost” in the background noise at a variety of frequency levels. As a guide for the interpretation of which frequencies have meaningful values for both the direction projections shown in the top three rows, and the phase velocities shown in the bottom row of Figure **3**, the cyclotron frequencies for both Oxygen and Hydrogen are shown by the cyan and magenta dashed lines in both Figures **2** & **3** in order to more readily identify regions having significant amplitudes for all six electromagnetic components.

4 Wave Vector Analysis for Unusual Disperion Events

4.1 A Region of Unusual Dispersion

Figure **4** of the present work shows the scalograms from a single data burst acquired shortly before the burst scalograms shown in Figure **9** of (Bennett 2023). In this figure, the arrival times of EMPs from every lightning strike detected by the WWLLN are shown by the vertical dashed white lines. Not a single normally dispersed whistlers is observed during this data burst. This data has the character described in (Bennett 2023) for periods that the Van Allen probe is passing through a plasma bubble. In the first half of the data shown, there are a great number of dispersionless spikes seen in the electric field scalograms, most of which do not have corresponding well isolated spikes substantially above the ambient clutter noise from the ubiquitous slow magnetosonic waves (Bennett 2023) in the magnetic field scalograms, so that a wavevector analysis of the sort described for Figure **3** is not feasible. The number of spikes is much greater than the number of detected WWLLN strokes during this period. Furthermore, the timing of the WWLLN stroke arrivals do not line up well with the strong dispersionless spikes in the VAP data. Since the wavevector analysis shown above in Figure **3** relies on having scalogram amplitudes for all six electric and magnetic field components that are reasonably stronger than the surrounding “noise” of other waves, the region indicated by the bracket with arrows labeled “Period of Interest” has been chosen for further wavevector analysis because of the intense dispersionless spikes in the magnetic field scalograms. This region is also of interest as it appears to be at the edge of a plasma bubble, since the dispersionless spikes are suddenly not seen after this period.

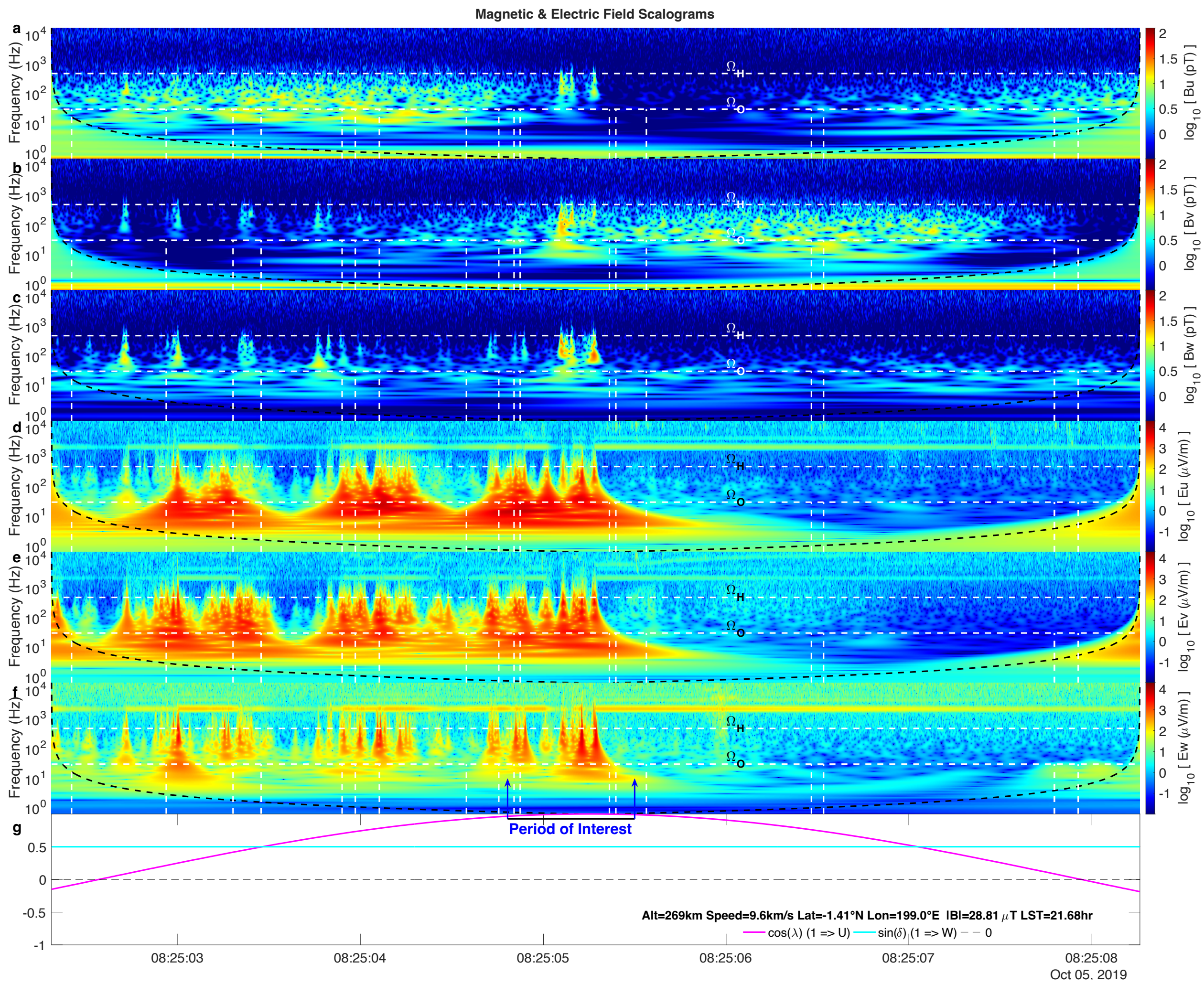

Figure 4. Scalograms of the three magnetic and electric field components in the spinning U,V, W reference frame are displayed for a single burst of data. The white dashed vertical lines are plotted at the times of the arrival at the subsatellite location for every WWLLN event detected during this data burst. In **a**, **b** and **c**, scalograms for the Bu, Bv and Bw components of the magnetic field are shown. In **d**, **e** and **f**, scalograms for the Eu, Ev and Ew components of the electric field are shown. In **g**, the satellite spin vector coordinates λ and δ, characterizing the orientation relative to the local magnetic field, are indicated over the course of this data burst.

4.2 Scalograms from A Region of Unusual Dispersion and the Cone of Influence

Figure **5** shows in more detail scalograms of the three magnetic and electric field components for the bracketed region indicated in Figure **4**. Superposed on the scalograms are eight white vertical dashed lines labeled #1 - #8 chosen to pass through peaks in either the magnetic or electric scalograms. The four dashed red vertical lines are drawn at the expected arrival times of the peaks of LG waves at the subsatellite location, using the WWLLN measured locations and strike times assuming a propagation speed through the EIWG of 235 km/s. For other cases (not shown here) involving clear normal whistler observations, the 235 km/s speed accurately predicts the arrival time for LG waves at the subsatellite location. For each of the four

WWLLN detected waves, the angular distance from the subsatellite point to the WWLLN determined strike location is indicated in **5f** by the blue text numbers.

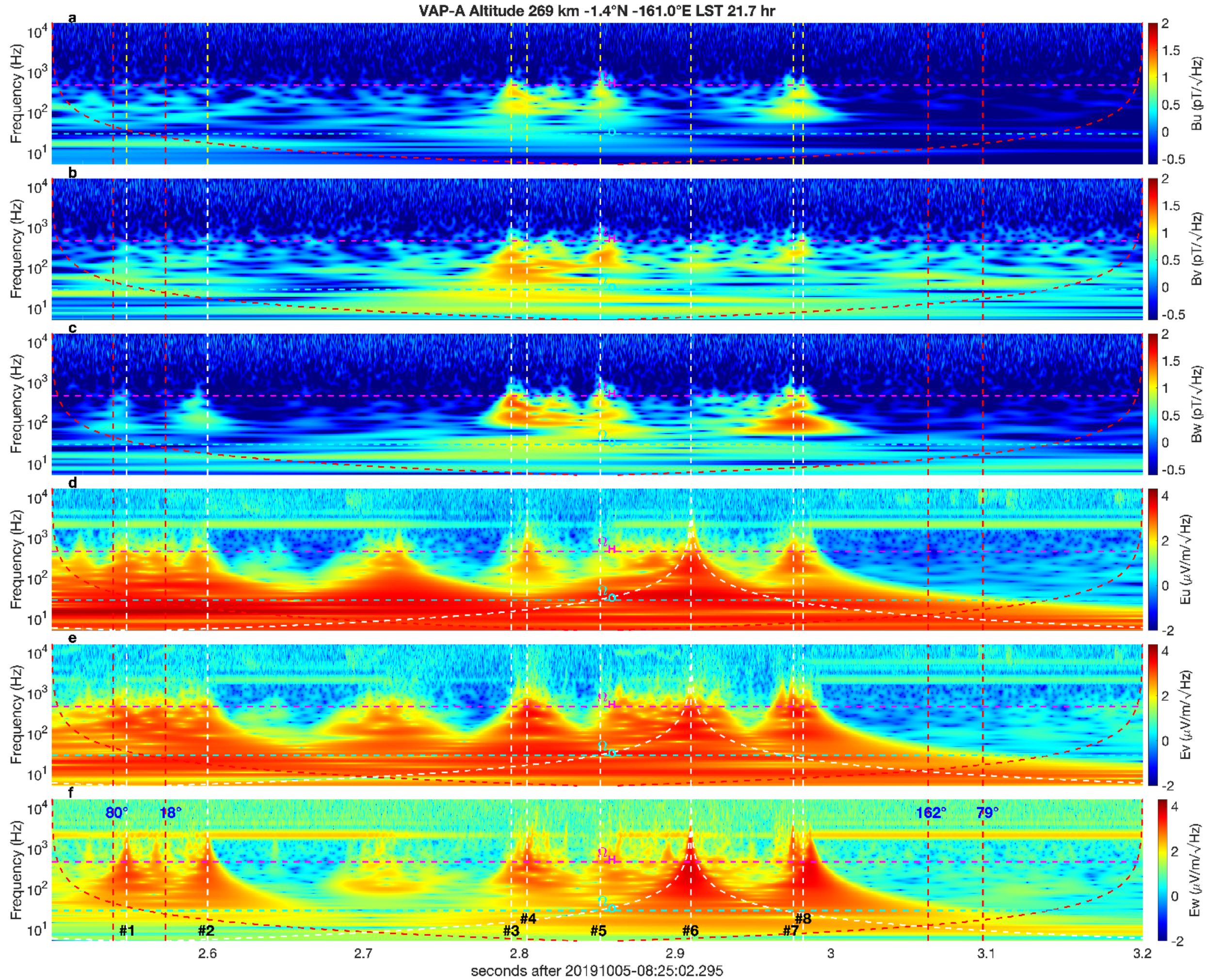

Figure 5. Scalograms from a subset of the time range in the previous figure are shown here. In **a**, **b** and **c**, scalograms of the three magnetic field components are shown. In **d**, **e** and **f**, scalograms of the three electric field components are shown.

The noisiness of the following wavevector analysis for propagation direction and phase velocity may be attributed to the variability in the contributions from the numerous other waves present at the times chosen for analysis. The cone of influence (COI) shown by the curved red dashed lines superimposed over the scalogram plots in Figure **5** indicates the division between lower frequencies for which the continuous wavelet transformation is affected by the boundaries at the start and end of the data sample and higher frequencies that are not affected. The COI represents the "confusion time range" over which other waves contribute to the scalogram amplitudes associated with a given peak. For example, the strongest spike in the electric field scalograms, labeled #6, spreads more broadly in time at lower frequencies just as does the COI shown by the curved white dashed line in **5d**, **5e** and **5f**.

4.3 Time Resolved Waveforms from A Region of Unusual Dispersion

Figure **6** shows the time resolved functions of the electric and magnetic field component values over the same time interval as the previous figure, together with the Nickolaenko (2004) model for the radial electric and azimuthal magnetic field strengths computed using the WWLLN detected locations, times and intensities.

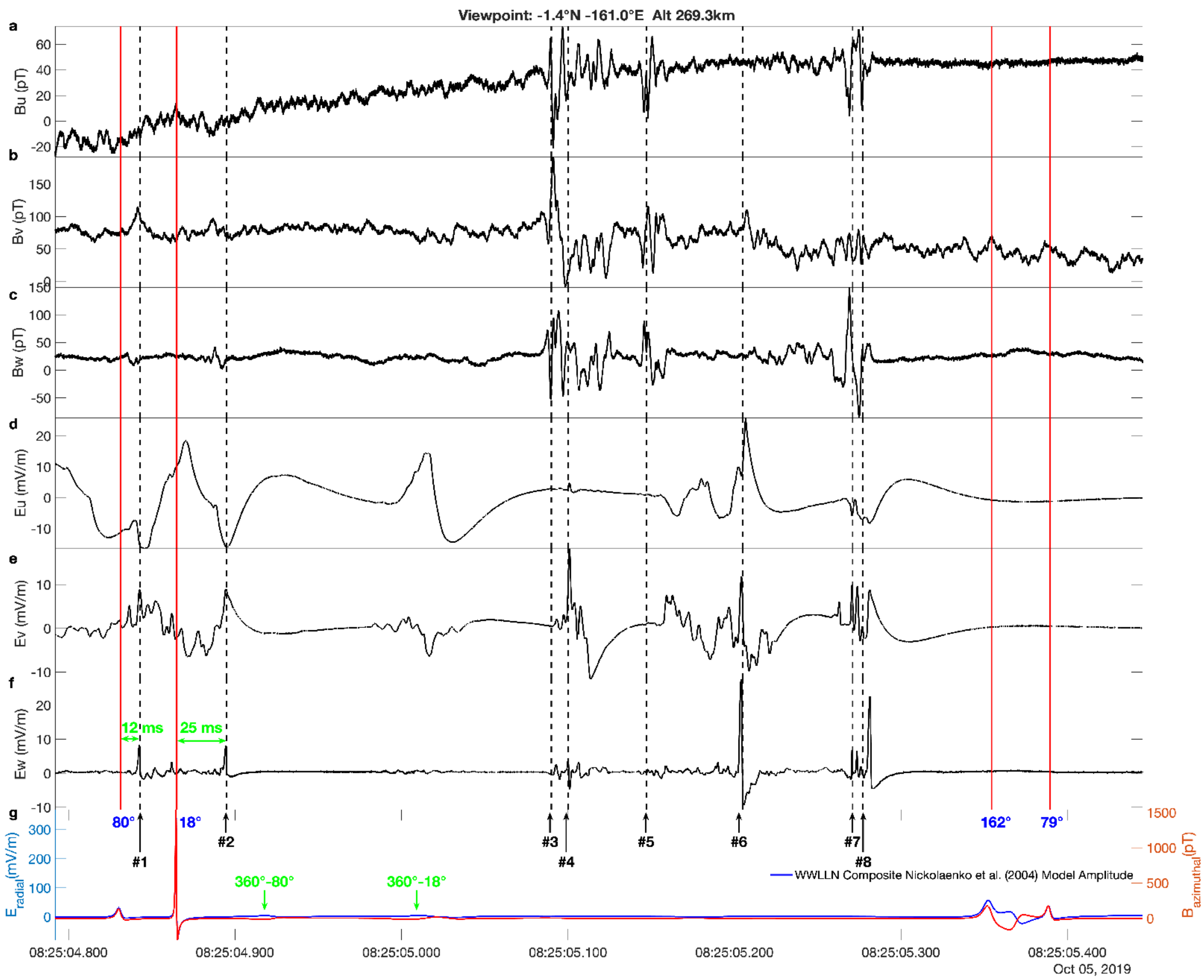

Figure 6. Time resolved waveforms for the electric and magnetic field components are shown. In **a**, **b** and **c**, the three magnetic field components are shown. In **d**, **e** and **f**, the three electric field components are shown. In **g** the intensities of the azimuthal electric and magnetic field amplitudes at the subsatellite point according to the Nickolaenko et al. (2004) model using the WWLLN measured stroke energies, times and locations are plotted. The angular distance from each WWLLN stroke to the subsatellite point are indicated in **g** by the blue text numbers.

As seen in Figure **6g**, several *model* LG pulses, using the four WWLLN locations and intensities of individual lightning strokes, are expected to arrive over the time period shown. The strongest peak at 8:25:04.865 originates from a strike at an angular distance of 18° from the subsatellite. In Figure **6g**, both the time resolved model radial electric and azimuthal magnetic fields are shown using the WWLLN measurements. The model also shows significant broad peaks at the times corresponding to waves travelling around the globe in the opposite direction from the primary peaks (indicated by the 360°-80° and 360°-18° green labels in Figure **6g**). Note that nearby strikes have much narrower peaks in the model than more remote strikes. It is clear that there are many more peaks in the electric and magnetic amplitudes in Figure **6a** through **6f** than the number of WWLLN detected lightning strokes.

4.4 WWLLN vs. GLM detections

The WWLLN detection efficiency is known (Holzworth et al., 2019) to decrease substantially for lightning strokes having peak currents below 50 kA. The WWLLN is also approximately twice as efficient (Abarca et al., 2010; Holzworth et al., 2019) for the detection of cloud-ground strokes than for in cloud events. Because the WWLLN measured stroke energies are directly proportional to the far field VLF energy radiated from lightning events, these energies can be used with the (Nickolaenko, et al. 2004) model predict the amplitude of the electric and magnetic fields at the subsatellite location, as discussed in (Bennett 2023) and as shown in Figure **6g** of the present work.

In contrast, the Geostationary Lightning Mapper (GLM) (Bateman et al., 2020; Goodman et al., 2013; Rudlosky et al., 2019) detects lightning flashes using optical observations. A lightning flash, according to (Goodman et al., 2012), consists of "groups" of "events" located within 0.15° arc distance and no more than 330 s difference in time between the groups in a flash. The GLM measured optical intensity is not directly proportional to the far field VLF-ELF intensity. For example, a primarily horizontal transfer of charge sufficient to produce significant GLM signals, as may occur in some in-cloud events, would produce negligible far field VLF-ELF radiation compared to a primarily vertical transfer of charge as expected for cloud-ground events. For this reason, the GLM optical intensity measurements cannot be used to predict the observed strength of the electric and magnetic field variations by the Van Allen probe instruments.

In Figure **7**, the location, times and intensities of every lightning event detected by either the WWLLN, the GLM or both are shown over the time period of interest indicated in Figure **4**. Figure **7a** displays the locations of these events, with superposed text showing the distance to the Van Allen Probe-A satellite. WWLLN locations are shown by green circles, while GLM locations are shown by red circles. Matches between WWLLN and GLM flashes are shown by blue X marks. The numbers for each category of flash are shown in the title of Figure **7a**. The same color coding for locations is used for the distance indications in the superposed text. In Figure **7b** the WWLLN measured energies are plotted as a fuction of the time for each detected event. In Figure **7d** the GLM measured group optical energies are plotted as a fuction of the time for each individual group. In Figure **7c** the GLM measured flash optical energies, given by the sum of the energies of each group in a given flash, are plotted as a fuction of the time for each flash. Where both GLM and WWLLN detections coincide in time and space, the timing of the WWLLN flash usually agrees best with the earliest GLM group in a flash. For this reason, the time plotted for every GLM flash is displayed as the time of the first group in that flash.

Since the coupling to the far field EMP waveforms at a distant location from an individual GLM group at the very least contains a factor:

$$Farfield\ Factor = \cos\left(\theta_{charge-transfer}\right), \tag{6}$$

that depends on the angle of the charge transfer moment with respect to the vertical direction, and since this angle is not determined in the GLM data processing, the expected farfield waveforms may have either positive or negative signs, and may be significantly less in magnitude than for purely vertical charge transfer events. Cloud-Ground strokes would tend to have larger farfield factors (FFFs) than cloud-cloud strokes. If this factor is relatively small, it can explain the lack of detection by the WWLLN of groups that appear strong in the GLM data.

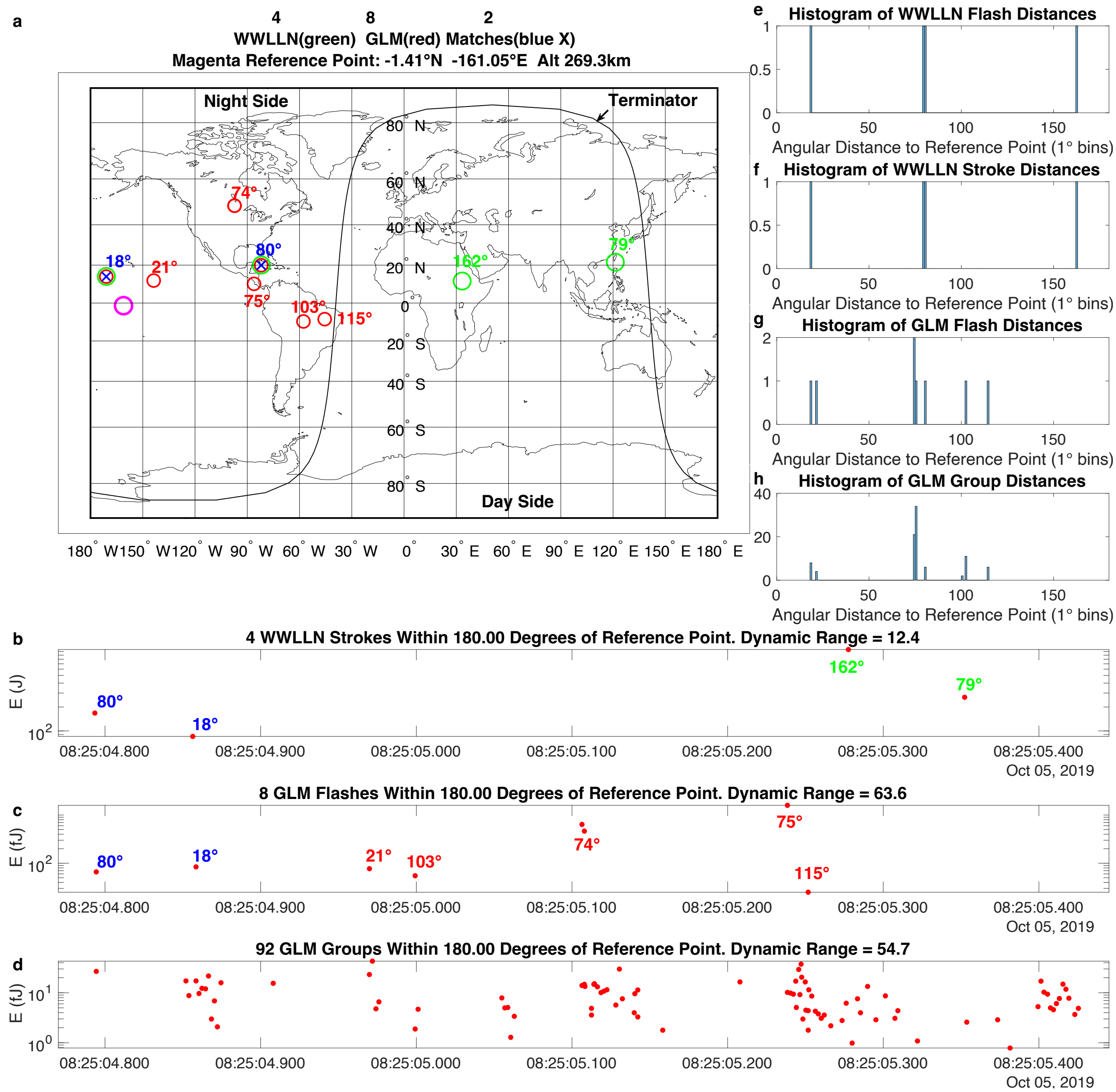

Figure 7. The locations, times and intensities of lightning detections are shown over the time period of interest.

4.5 GLM groups and EMIFISIS observations

Regardless of the resulting strength of farfield LG EMPs from the FFFs, the expected arrival times for each GLM group at the subsatellite location may be precisely estimated from the angular distance using a propagation speed of approximately 235 km/s through the EIWG. In Figure **8**, these predicted times are plotted over the scalograms of the three electric field components over the time period of interest shown in Figure **4**. In some cases, such as the first two peaks detected by both the WWLLN and the GLM, labeled by the 80° and 18° angular distances from the subsatellite point, there are clearly identifiable delays corresponding to the travel up through the ionosphere to the EMFISIS detectors, viz. 12 ms and 25 ms respectively as shown in Figure **8f**. For most of the peaks seen the electric field amplitudes in Figure **8**, the identification of the source LG event is ambiguous.

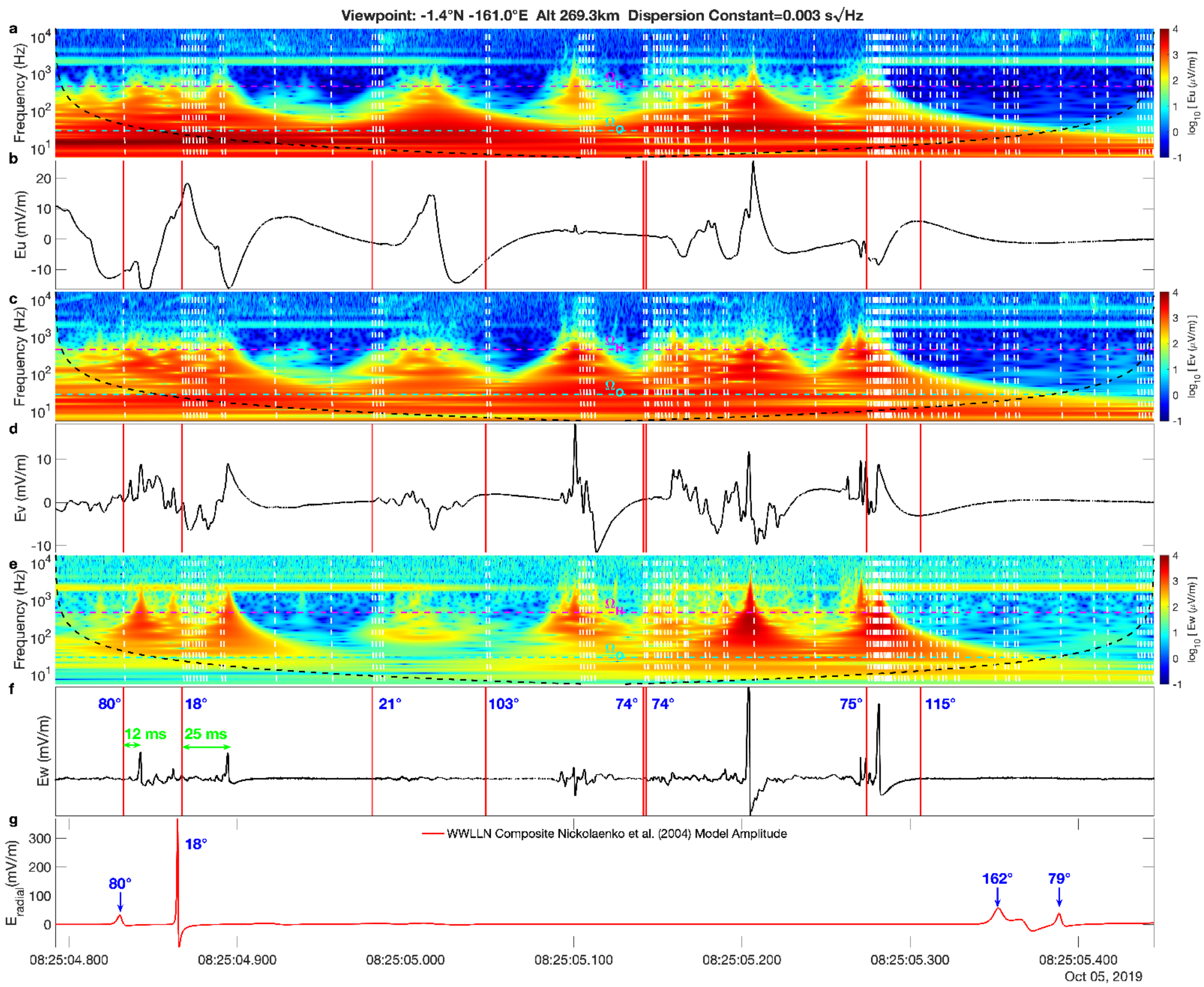

Figure 8. The locations and times of lightning detections are compared with VAP data.

4.6 Wavevector Analysis of a Region of Unusual Dispersion

In cases where all three components of the spectrally resolved magnetic field are available, singular value decomposition methods (Santolik et al. 2003) may be used to determine the wavevector $\boldsymbol{k}$. Figure **9** displays the scalar product of the unit wavevector $\widehat{\boldsymbol{k}}$ with each of the three MFA directions as a function of both time and frequency over the time period indicated in Figure **4**. Also shown is the RPA estimate for the phase velocity (Bennett 2023) as a function of time and frequency.

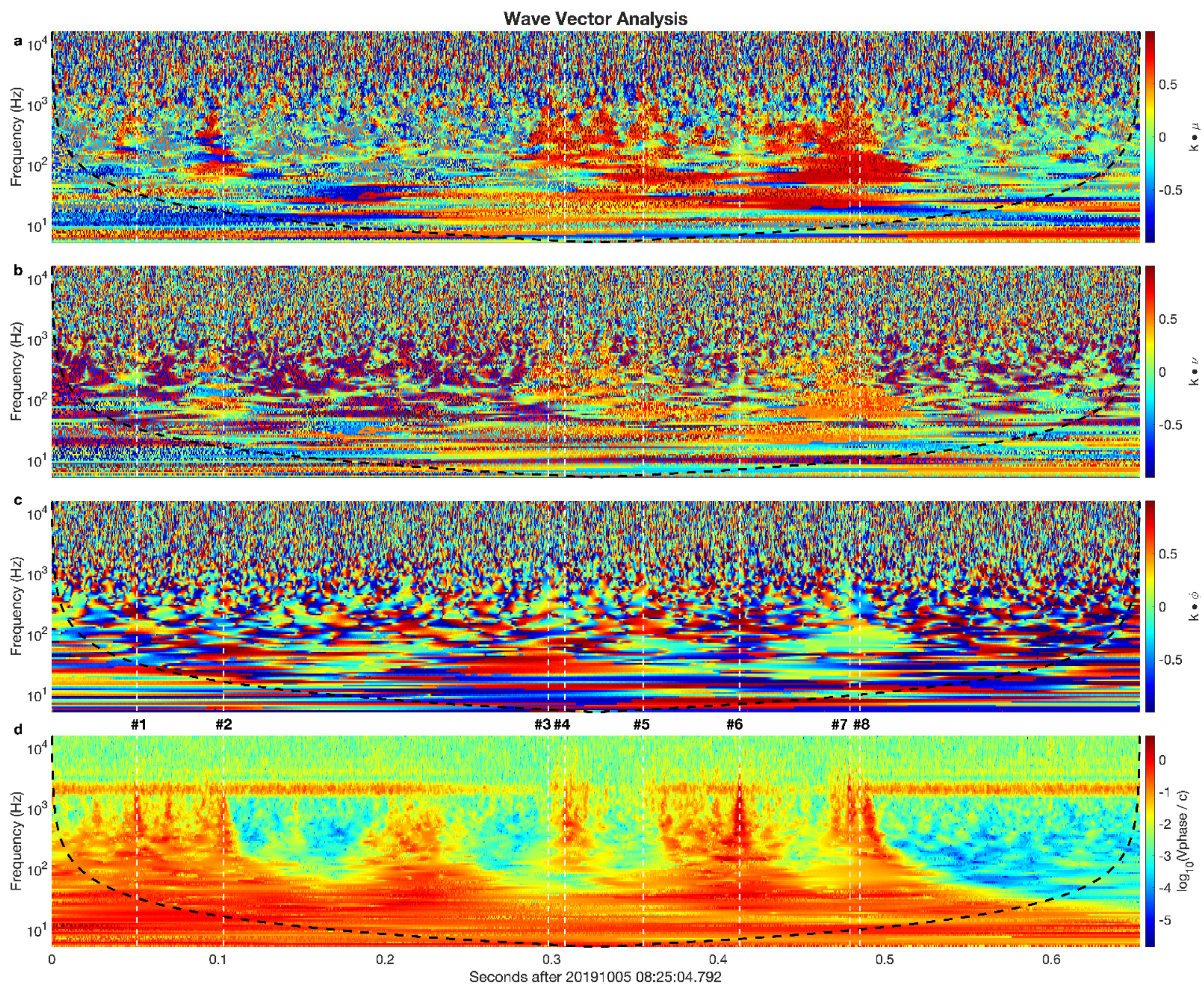

Figure 9. The direction cosines between the unit wavevector $\widehat{\boldsymbol{k}}$ and the three MFA coordinates are shown as a function of time and frequency. In **a**, **b** and **c**, the projections on the directions μ, ν and ϕ respectively are shown. In **d**, the logarithm of the phase velocity relative to the speed of light is shown.

4.7 Energy Propagation Analysis of a Region of Unusual Dispersion

Figure **10** displays the scalar product of the Poynting vector ***S*** with each of the three MFA directions over the time period shown in Figure **4**. Note that some of the times having the strongest energy flow, e.g. case #6 in Figure **10**, do not have significant magnetic field components, so that the unit wavevector projections in Figure **9** do not show a clear peak at this time. On the other hand, some of the times having clear direction cosines available in Figure **9**, e.g. case #5, have only very weak Poynting vector signals in Figure **10**. Also shown in Figure **10d** is the crude estimate of phase velocity derived from the ratio of the electric to magnetic field intensity. Although this crude estimate is not as accurate as the RPA estimate shown in Figure **9d**, it does not require determination of the wavevector.

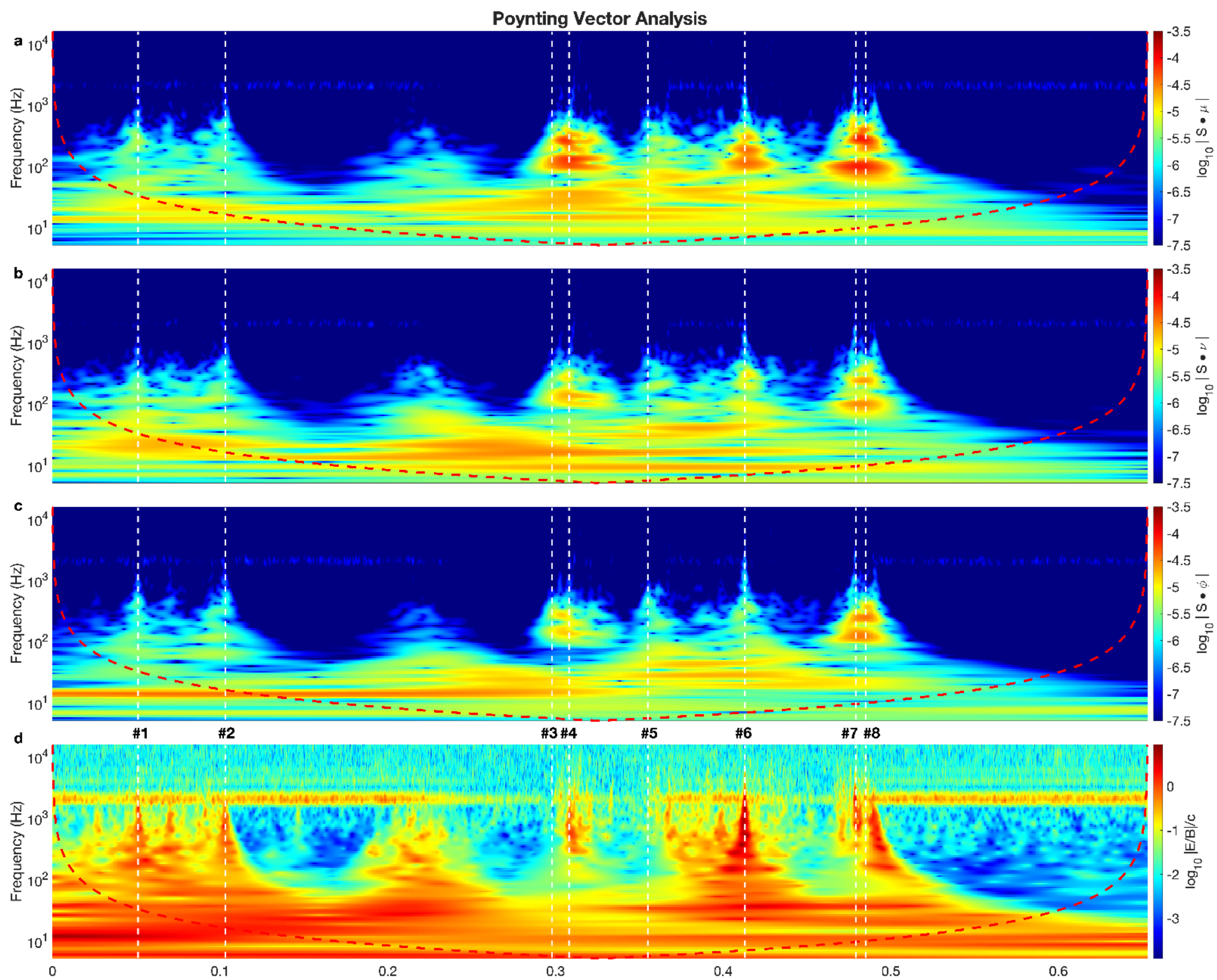

Figure 10. The absolute values of the scalar product of the Poynting vector ***S*** and the three MFA coordinates are shown as a function of time and frequency. In **a**, **b** and **c**, the projections on the directions μ, ν and ϕ are shown respectfully. In **d**, the composite azimuthal magnetic field amplitude is plotted according to the Nickolaenko et al. (2004) model using the WWLLN measured stroke energies, times and locations. The angular distance from each individual WWLLN stroke to the subsatellite point are identified in **d** by the blue text numbers.

The unit wavevector $\hat{\boldsymbol{k}}$ direction cosines displayed in Figure **9** show that the five pulses labeled #3, #4, #5, #7 and #8 in **7c**, are travelling in approximately the same direction while the pulses labeled #1, #2 and #6 have results too noisy for clear evaluation. The direction cosines in Figure **9a** are close to unity along the magnetic field direction for the five pulses, while being close to zero along the ~vertical (Figure **9b**) and Eastward (Figure **9c**) directions. The similar color patterns seen for the three unit Poynting vector direction cosines in Figures **10a**, **10b** and **10c** for cases #4, #6, #7 and #8 show that the energy flow is also reasonably well aligned with the magnetic field direction for these four cases.

Another metric for the degree of confusion is the homogeneity of the color in plots of the unit wavevector direction cosines shown in Figures **9a**, **9b** and **9c**. In Figure **9a** for example, for most frequencies below 3 kHz, the reddish color indicates a direction well aligned with the local magnetic field, while the graininess of the color above 300 Hz in Figure **9b** indicates significant noise in the projections along the nearly vertical ν direction, while around 100 Hz, the orangish color indicates a vertical component of the unit wavevector has a value of approximately 0.4 for the direction cosine.

4.8 Foamy Behavior of Unusual Dispersion Regions

The wavevector analysis in Figure **11** for cases labeled #3, #4, #5 and #8 in the earlier figures displays an unusual phase velocity distribution. At frequencies below the local oxygen cyclotron frequency, the RPA estimated phase velocity is approximately 30 Mm/s for all four cases. For cases #3 and #5, above the oxygen cyclotron frequency the RPA phase velocity drops to approximately 2 Mm/s and *is approximately constant*. In contrast, cases #4 and #8 in the 2nd and 4th columns, appear to alternate between 2 Mm/s and 30 Mm/s regions. Cases #4 and #8 correspond to spikes having the greatest Poynting vector flux, as seen in Figure **10**. Apparently large Poynting flux values are associated with higher phase velocities.

The results displayed in Figures **11e** and **11o** are in stark contrast to the normal variation of phase velocity as a function of frequency seen in Figures **3e**, **3j**, **3o** and **3t**. In the Figure **11e** and **11o** plots the constancy of the phase velocity above the relevant local cyclotron frequency, Oxygen in this case, cannot be explained by any normal IRI model. In general, the local plasma dispersiveness produces a phase velocity increasing as the square root of the frequency, as shown in Figure **1** of (Bennett 2023) or in Figure **3** of the present work. Evidence that the phase velocity for these waves is not merely locally dispersionless, but also nearly dispersionless along their full path through the ionosphere to the satellite is simply that the appearance in the scalograms such as in Figures **4** or **5** is of purely vertical spikes with negligible indication of dispersion, *despite substantial overall propagation delays*.

The ionospheric length of the propagation path followed by LG waves cannot be less than a purely vertical path of approximately 100 km from the EIWGUB to the satellite, and thus the propagation delays of 12 and 25 ms for the first two LG events in Figure **8**, correspond to speeds no less than 8 and 4 Mm/s respectively. These speeds have the same order of magnitude as the RPA estimates shown in the last row of plots in Figure **11**.

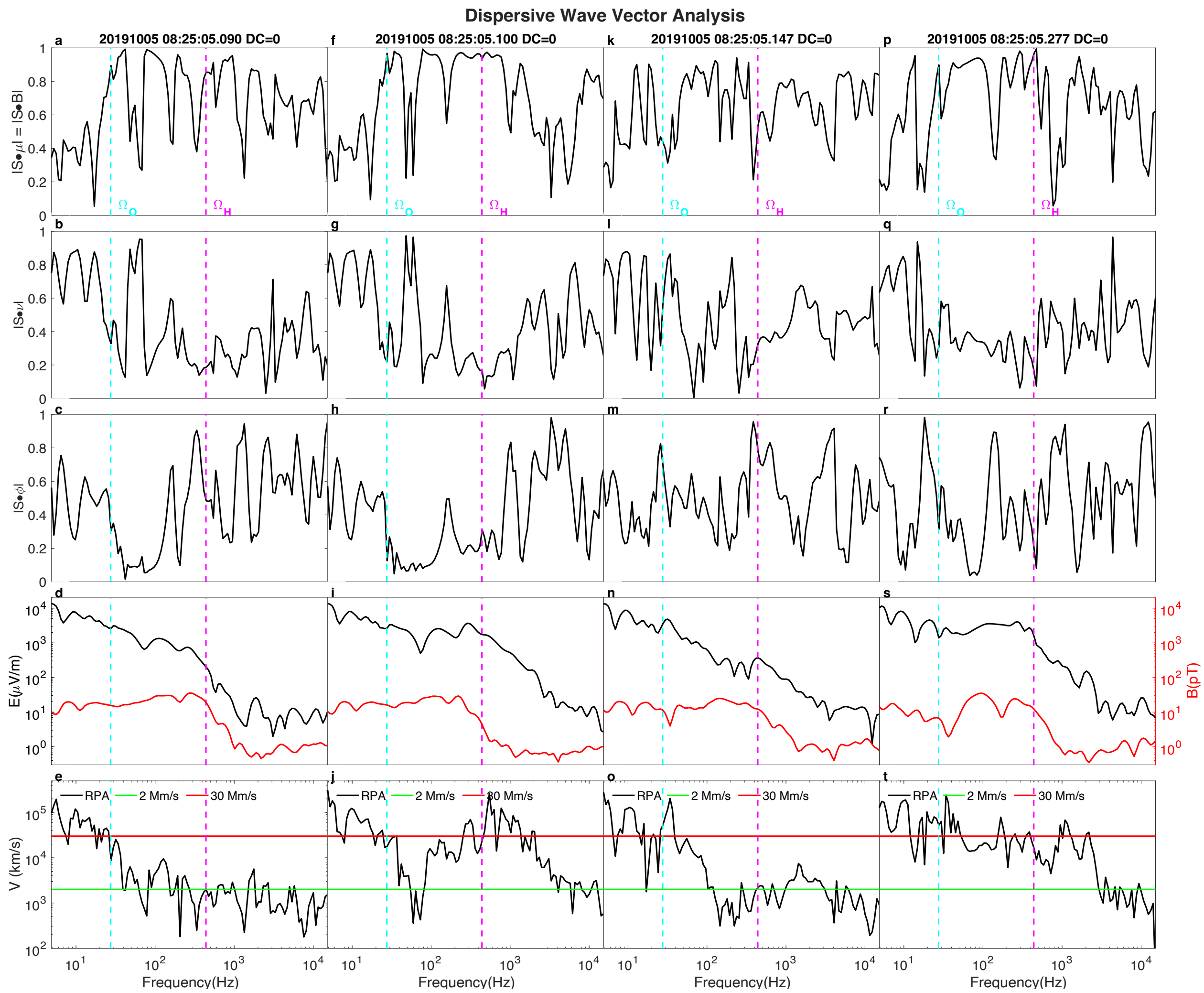

Figure 11. A wavevector analysis with the same layout as that displayed in Figure **3** is shown here for the four times indicated in Figure **6f** by vertical dashed lines and numbered #3, #4, #5 and #8.

5 Discussion and Conclusions

The suggestion that the roots of plasma bubbles are foamy is not based on detailed observations of the spatial structure of the bubbles, but rather on the propagation characteristics of EMPs passing through them. Most significant is the frequency independent phase velocity (i.e. dispersionless) behavior observed for certain events in wavevector analysis when all three magnetic and electric field components are available. Less significant, but more readily observed in cases for which significant magnetic field variations corresponding to the electric field variations are not available, is the dispersionless behavior implied by the almost perfectly vertical extension of scalogram peaks that may be substantially delayed relative to the parent lightning stroke. Such behavior is characteristic of acoustic wave propagation through liquid/vapor foams.

Another aspect of the "foamy" behavior is the strong attenuation of EMPs. This effect is more difficult to prove directly with the Van Allen probe observations. In some rare cases, such as the unusual lightning flash discussed in (Bennett 2023), multiple intense strokes of lightning are seen emerging from a single location that may be identified with individual LG pulses measured by the Van Allen probe detectors. In this case, with nearly identical paths traversed from source to detector, the correlation between propagation delay and attenuation may be made. A more indirect manifestation of the strong attenuation of LG waves passing through such hypothetical foamy plasma is the fact that most lightning strokes do not produce detectable whistler events in the Van Allen probe data.

In (Zheng et al., 2015) a search for coincident detections of LG events by the Van Allen probe satellites and the WWLLN was made. For the subset of lightning strikes within 18° of the subsatellite location, only 15.3% of the strikes were detected by the Van Allen probe instruments. The relatively low 15% coincidence rate found in this study could be explained by the presence of underlying plasma bubble foam covering approximately 85% of the bottom of the ionosphere. In (Jacobson et al., 2018) it was found that most lightning strokes were not detected by the C/NOFS instruments, while occasionally there was greatly enhanced transmission of LG waves to the satellite. Quantitatively, from line 6 of table 1 of (Jacobson et al., 2018) listing a population of 136-thousand WWLLN strokes having predicted strong Poynting-fluence at the subsatellite point, the estimated number of coincident VEFI whistlers, from line 13 of table 1 was only 19-thousand (14%). These authors suggested that km-scale D-layer irregularities might be responsible for these effects. Frequently appearing foamy plasma bubble roots of the sort discussed here could explain both the lack of detection for most lightning strokes noted by (Jacobson et al., 2018) and the occasional greatly enhanced transmission. The rare enhanced transmission observations would correspond to cases for which the C/NOFS satellite was either immersed in, or just above, a plasma bubble root, while the more common lack of detection would correspond to foamy, strongly attenuating bubbles not extending up to the C/NOFS satellite that effectively absorbed most of the LG energy. Despite the quite different analysis approaches of (Zheng et al., 2015) and (Jacobson et al., 2018), their coincident rates between satellite observations of whistlers and WWLLN detected lightning strokes are in reasonable agreement.

In conclusion, it is suggested that most (~80%) of the bottom of the nocturnal equatorial ionosphere is covered with a "foamy" layer of plasma bubbles that extend contiguously down to neutral atmosphere. Whether this foam is turbulent is an open question. The detailed spatial structure of this foam is an open question. The possibility of two-phase foamy structure at the base of the ionosphere may complicate theoretical analyses that implicitly assume a single-phase medium. Many other such questions remain open, but it is hoped that follow up observations and theoretical analysis might be stimulated by the present suggestions.

Acknowledgments

This work is entirely self funded by the author. WWLLN data was purchased from the University of Washington (https://wwlln.net). Van Allen Probe wave data used in this paper can be found in the EMFISIS archive (http://emfisis.physics.uiowa.edu/data/index) and the work of the EMFISIS team in its production is gratefully acknowledged. GLM data is available from the Geostationary Operational Environmental Satellites-R Series web site (https://www.goes-r.gov).

References

Abarca, S.F., Corbosiero, K.L., & Galarneau, T.J. Jr. (2010). An evaluation of the Worldwide Lightning Location Network (WWLLN) using the National Lightning Detection Network (NLDN) as ground truth. *Journal of Geophysical Research, 15*, D18206, doi:10.1029/2009JD013411

Abdu, M.A., Batista, I.S., Reinisch, B.W., MacDougall, J.W., Kherani, E.A., & Sobral, H.H.A (2012). Equatorial range spread F echoes from coherent backscatter, and irregularity growth processes, from conjugate point digital ionograms., *Radio Science*, 47, RS6003, doi:10.1029/2012RS005002

Balan, N., Liu, LiBo & Le, H. (2018). A brief review of equatoial ionization anomaly and ionospheric irregularities. *Earth and Planetary Physics, 2*, 257-275, doi:10.26464/epp2018025

Bateman, M., Mach, D., & Stock, M. (2020). Further investigation into detection efficiency and false alarm rate for the geostationary lightning mappers aboard GOES-16 and GOES-17. *Earth and Space Science, 8*, 2020EA001237. https://doi.org/2020EA001237

Bennett, C.L. (2023). A Novel Population of Slow Magnetosonic Waves and a Method for the Observation of the Roots of Plasma Bubbles in the Lower Ionosphere. *ESS Open Archive*. January 17, 2023, doi:10.1002/essoar.10511954.3

Chou, M.Y., Yue, J., Sassi, F., Huba, J., McDonald, S.E., Tate, J.L., et al, (2022). Modeling the Day-to-Day Variability of Midnight Equatorial Plasma Bubbles with SAMI3/WACCM-X. Authorea. December 27, 2022, doi:10.22541/essoar.167214177.74303978/v1

De Jonghe, J. & Keppens, R. (2020a). A two-fluid analysis of waves in a warm ion-electron plasma. *Plys. Plasmas*. *27*, 122107, doi:10.1063/5.0029534

De Jonghe, J. & Keppens, R. (2020b). Two-Fluid Treatment of Whistling Behavior and the Warm Appleton-Hartree Extension. *Journal of Geophysical Research: Space Physics, 126,* e2020JA028953, doi:10.1029/2020JA028953

De Michelis, P., Consolini, G., Alberti, T., Tozzi, R., Giannattasio, F., Coco, I., et al. (2022). Magnetic Field and Electron Density Scaling Properties in the Equatorial Plasma Bubbles. *Remote Sens. 14*, 918, doi:10.3390/rs14040918

De Michelis, P., Consolini, G., Tozzi, R., Pignalberi, A., Pezzopane, M., Coco, I., et al. (2021). Ionospheric Turbulence and the Equatorial Plasma Density Irregularities: Scaling Features and RODI. *Remote Sens. 13*, 759, doi:10.3390/rs13040759

Goodman, S., Blakeslee, R., Koshak, W., Mach, D., Bailey, J., Buechler, D., et al. (2013). The goes-r Geostationary Lightning Mapper (GLM). *Atmospheric Research, 125-126*, 34-49, doi:10.1016/j.atmosres.2013.01.006

Goodman, S., Mach, D., Koshak, W., Blakeslee, R. (2012). Algorithm theoretical basis document: GLM lightning cluster-filter algorithm. Version 3.0. July 30, 2012. NOAA NESDIS Center for satellite applications research.

Heelis, R. (2004). Electrodynamics in the low and middle latitude ionosphere: A tutorial. *Journal of Atmospheric and Solar-Terrestrial Physics, 66*(10), 825-838, doi:10.1016/j.jastp.2004.01.034

Holzworth, R.H., McCarthy, M.P., Brundell, J.B., Jacobson, A.R. & Rodger, C.J. (2019). Global distribution of superbolts. *Journal of Geophysical Research: Atmospheres, 124*, 9996-10,005, doi:10.1029/2019JD030975

Huba, J.D. (2023). Resolution of the equatorial spread F problem: Revisited. *Front. Astron. Space Sci.* 9:1098083, doi:10.3389/fspas.2022.1098083

Hysell, D.L., Larsen, M.F., Swenson, C.M., Barjatya, A., Wheeler, T.F., Sarango, M.F., et al. (2005). Onset conditions for equatorial spread F determined during EQUIS II. *Geophysical Research Letters*, *32* (L24104), doi:10.1029/2005GL024743

Immel, T.J., Mende, S.B., Frey, H.U., Peticolas, L.M., & Sagawa, E. (2003). Determination of low latitude plasma drifts speeds from FUV images. *Geophysical Research Letters, 30*(18), 1945, doi:10.1029/2003GL017573

Jacobson, A.R., Holzworth, R.H., Pfaff, R. & Roderick H. (2018). Coordinated Satellite Observations of the Very Low Frequency Transmission Through the Ionospheric D Layer at Low Latitudes, Using Broadband Radio Emissions from Lightning. *Journal of Geophysical Research: Space Physics, 123*, 2926-2952, doi:10.1002/2017JA024942

Kelley, M.C., Makela, J.J., de La Beaujardiere, O., & Retterer, J. (2011). Convective Ionospheric Storms: A Review. *Rev. Geophys., 49*, RG2003, doi:10.1029/2010RG000340

Karan, D.K., Daniell, R.E., England, S.L., Martinis, C.R., Eastes, R.W., Burns, A.G., & McClintock, W.E. (2020). First zonal drift velocity measurement of equatorial plasma bubbles (EPBs) from a geostationary orbit using GOLD data. *Journal of Geophysics: Space Physics 125*, e2020JA028173, doi:10.1029/2020JA028173

Kil, H., Demajistre, R., & Paxton, L.J. (2004). F-region plasma distribution seen from TIMED/GUVI and its relation to the equatorial spread F activity. *Journal of Geophysical Research, 31*, L05810, doi:10.1029/2003GL018703

Kil, H., & Heelis, R.A. (1998). Global distribution of density irregularities in the equatorial ionosphere. *Journal of Geophysical Research, 103*, 407-417 doi:10.1029/97JA02698

Kil, H., Sun, K.A., Chang, H., Paxton, L.J., Nikoukar, R., & Lee, J. (2022). Characteristics and sources of electron density irregularities near and after midnight in the equatorial F region. Oral presentation SA55A-03 at AGU fall meeting, Chicago Illinois, USA. https://agu.confex.com/agu/fm22/meetingapp.cgi/Paper/1177560

Kudeki, E., & Bhattacharyya, S. (1999). Postsunset vortex in equatorial F-region plasma drifts and implications for bottomside spread F. *Journal of Geophysical Research*, 104(A12), 28, 163-28, 170, doi:10.1029/1998JA900111

Liang, J., Donovan, E., Jackel, B., Spanswick, E. & Gillies, M. (2016) On the 630 nm red-line pulsating aurora: Red-line Emission Geospace Observatory observations and model simulations. *Journal of Geophysical Research: Space Physics, 121*, 79880-8012, doi:10.1002/2016JA022901

Makela, J.J., & Kelley, M.C. (2003). Field-aligned 777.4-nm composite airglow images of equatorial plasma depletions. *Geophysical Research Letters, 30*(8), 1442, doi:10.1029/2003GL017106

Makela, J.J., Kelley, M.C., & Nicolls, M.J. (2006). Optical observations of the development of secondary instabilities on the eastern wall of an equatorial plasma bubble, *J. Geophys. Res., 111*, A09311, doi:10.1029/2006JA011646

Makela, J.J. & Miller, E.S. (2008). Optical observations of the growth and day-to-day variability of equatorial plasma bubbles, *J. Geophys. Res., 113*, A03307, doi:10.1029/2007JA012661

Makela, J.J. & Otsuka, Y. (2012). Overview of Nighttime Ionospheric Instabilities at Low- and Mid-Latitudes: Coupling Aspects Resulting in Structuring at the Mesoscale. *Space Sci. Rev 168*, 419-440, doi:10.1007/s11214-011-9816-6

Martinis, C., Eccles, J.V., Baumgardner, J., Manzano, J., & Mendillo, M. (2003). Latitude dependence of zonal plasma drifts obtained from dual-site airglow observations. *Journal of Geophysical Research, 108*(A3), 1129, doi:10.1029/2002JA009462

Mendillo, M., & Baumgardner, J. (1982). Airglow characteristics of equatorial plasma depletions. *Journal of Geophysical Research, 87*(A9), 7641-7652, doi:10.1029/JA087iA09p07641

Min, K., Takahashi, K., Ukhorskiy, A.Y., Manweiler, J.W., Spence, H.E., Singer, H.J., et al. (2017), Second harmonic poloidal waves observed by Van Allen Probes in the dusk-midnight sector. *J. Geophys. Res. Space Physics, 122*, 3013-3039, doi:10.1002/2016JA023770

Narayanan, V.L., Sau, S., Gurubaran, S., Shiokawa, K., Balan, N., & Emperumal, K. (2014). A statistical study of satellite traces and subsequent evolution of equatorial spread F based on ionosonde observations over dip equatorial site Tirunelveli, India. *Earth, Planets and Space*, 676(1), 160, doi:10.1186/s40623-014-0160-4

Nickolaenko, A.P., & Rabinowicz, L.M. (2004). Time domain presentation for ELF pusles with accelerated convergence. *Geophysical Research Letters, 31*, L05808, doi:10.1029/2003GL018700

Patra, A.K., Yokoyama, T., Yamamoto, M., Saito, S., Maruyama, T. & Fukao, S. (2005). Disruption of E region echoes observed by the EAR during the development phase of equatorial spread F: A manifestation of electrostatic field coupling. *Geophysical Research Letters, 32*(L17104), doi:10.29/2005GL022868

Pierre, J., Guillermic, R., Elias, R., Drenckhan, W., & Leroy, V. (2013). Acoustic characterization of liquid foams with an impedance tube. *The European Physical Journal E 36*(113), doi:10.1140/epje/i2013-13113-1

Piggott, W.R. & Rawer, K. (1972). URSI Handbook of Ionogram Interpretation and Reduction, second Edition, Novermber 1972, WDC A, Report UAG-23. https://repository.library.noaa.gov/view/noaa/10404

Pimenta, A.A., Bittencourt, J.A., Fagundes, P.R., Sahai, Y., Buriti, R.A., Takahashi, H., & Taylor, M.J. (2003). Ionospheric plasma bubble zonal drifts over the tropical region: A study using OI 630 nm emission all-sky images. *Journal of Atmospheric and Solar-Terrestrial Physics, 65*(10), 1117-1126, doi:10.1016/S1364-6826(03)00149-4

Ripoll, J.F., Farges, T., Malaspina, D.M., Lay, E.H., Cunningham, G.S., Hospodarsky, G.B. et al. (2020), Analysis of Electric and Magnetic Lightning-Generated Wave Amplitudes Measured by the Van Allen Probes. *Geophysical Research Letters, 47*, e2020GL087503, doi:10.1029/2020GL087503

Ritter, P., Luhr, H., & Rauberg, J. (2013), Determining field-aligned currents with the Swarm constellation mission. *Earth Planets Space, 65*, 1285-1294, doi:10.5047/eps.2013.09.006

Rodriguez-Zuluaga, J., Stolle, C., Yamazaki, Y., Xiong, C., & England, S.L. (2020). A synoptic-scale wavelike structure in the nighttime equatorial ionization anomaly. *Earth and Space Science, 8*, e2020EA001529, doi:10.1029/2020EA001529

Rudlosky, S., Goodman, S., Virts, K., & Bruning, E. (2019). Initial Geostationary Lightning Mapper observations. *Geophysical Research Letters, 46*, 1097-1104, doi:10.1029/2018GL081052

Santolik, O., Parrot, M., & Lefeuvre, F. (2003). Singular value decomposition methods for wave propagation analysis. *Radio Science, 38*(1), 1010, doi:10.1029/2000RS002523

Shiokawa, K., Otsuka, Y., Ogawa, T., & Wilkinson, P. (2004). Time evolution of high-altitude plasma bubbles imaged at geomagnetic conjugate points. *Annales Geophysicae, 29*(9), 3137-3143, doi:10.5194/angeo-22-3137-2004

Sivakandan, M., Mondal, S., Sarkhel, S., Chakrabarty, D., Sunil Krishna, M., V. Upadhayaya, A.K., et al. (2021). Evidence for the in-situ generation of plasma depletion structures over the transition region of geomagnetic low-mid latitude. *Journal of Geophysical Research: Space Physics, 126*, e2020JA028837, doi:10.1029/2020JA028837

Tsunoda, R.T. (1983). On the generation and growth of equatorial backscatter plumes: 2. Structuring of the west walls of upwellings. *Geophysical Research Letters, 88*(A6), 4869-4874, doi:10.1029/JA088iA06p04869

Woodman, R.F. (2009). Spread F - an old equatorial aeronomy problem finally resolved? *Ann. Geophysics 27*(5), 1915-1934, doi:10.5194/angeo-27-1915-2009

Woodman, R.F. and Hoz, C.L. Radar Observations of F Region Equatorial Irregularities. *Journal of Geophysical Research, 81*(31), 5447-5466, doi:10.1029/JA081i031p05447

Yokoyama, T., Yamamoto, M., Otsuka, Y., Nishioka, M., Tsugawa, T., Watanabe, S., & Pfaff, R.F. (2011). On postmidnight low-latitude ionospheric irregularities during solar minimum: 1. Equatorial Atmosphere Radar and GPS-TEC observations in Indonesia. *Journal of Geophysical Research, 116*, A11325, doi:10.1029/2011JA016797

Zheng, H., Holzworth, R.H., Brundell, J.B., Jacobson, A.R., Wygant, J.R., Hospodarsky, G.B., Mozer, F.S., & Bonnell, J. (2015). A statistical study of whistler waves observed by Van Allen Probes (RBSP) and lightning detected by WWLLN. *Journal of Geophysical Research: Space Physics, 121*, 2067-2079, doi:10.1002/2015JA022010